

## Research Article

# Dissolution and Solubility of the $(\text{Ba}_x\text{Sr}_{1-x})\text{HAsO}_4\cdot\text{H}_2\text{O}$ Solid Solution in Aqueous Solution at 25°C and pH 2

Xuehong Zhang,<sup>1</sup> Yinian Zhu,<sup>1</sup> Caichun Wei,<sup>1,2</sup> Zongqiang Zhu,<sup>1</sup> and Zongning Li<sup>1</sup>

<sup>1</sup> College of Environmental Science and Engineering, Guilin University of Technology, Guilin 541004, China

<sup>2</sup> College of Light Industry and Food Engineering, Guangxi University, Nanning 530004, China

Correspondence should be addressed to Yinian Zhu; zhuyinian@glut.edu.cn

Received 2 October 2013; Accepted 27 January 2014; Published 17 March 2014

Academic Editor: Stefan Tsakovski

Copyright © 2014 Xuehong Zhang et al. This is an open access article distributed under the Creative Commons Attribution License, which permits unrestricted use, distribution, and reproduction in any medium, provided the original work is properly cited.

Six different members of the  $(\text{Ba}_x\text{Sr}_{1-x})\text{HAsO}_4\cdot\text{H}_2\text{O}$  solid solution were prepared and characterized, and then dissolution of the synthetic solids was studied at 25°C and pH 2 in a series of batch experiments for 4320 h. With the increase in the Ba/(Ba + Sr) mole fraction of the solids, the aqueous pH decreased and the aqueous barium concentration increased. The aqueous strontium and arsenic concentrations had the highest values at Ba/(Ba + Sr) = 0.21. The solubility products for  $\text{BaHAsO}_4\cdot\text{H}_2\text{O}$  and  $\text{SrHAsO}_4\cdot\text{H}_2\text{O}$  were calculated to be  $10^{-5.52}$  and  $10^{-4.62}$ , respectively. The corresponding free energies of formation were determined to be  $-1543.99 \pm 0.18$  kJ/mol and  $-1537.94 \pm 0.02$  kJ/mol. The solid solution had a minimum solubility product of  $10^{-5.61}$  at Ba/(Ba + Sr) = 0.82. The Guggenheim coefficients were determined to be  $a_0 = 1.55$  and  $a_1 = -4.35$ . The Lippmann diagram was a typical Lippmann diagram for a nonideal solid solution with a negative enthalpy of mixing. The system shows an “alloyotropic” minimum at the aqueous Ba/(Ba+Sr) activity fraction of 0.87 where the *solutus* and *solidus* curves meet. At the end of the dissolution experiment, the dissolution followed the saturation curve for the pure endmember  $\text{BaHAsO}_4\cdot\text{H}_2\text{O}$  and approached the intersection with the minimum stoichiometric saturation curve on the Lippmann diagram.

## 1. Introduction

Arsenic in natural waters is a worldwide problem. Arsenic has been known from antiquity to be highly toxic for animals and the majority of plants [1, 2]. Although arsenic has been classified at the top of the priority list of the most hazardous substances [3, 4], the crystal structures and the solubility as well as the thermodynamic properties of numerous arsenates remain poorly determined. This is an important handicap because an in-depth study of the arsenate behaviour in soils, sediments, and natural waters that have been subjected to pollution requires a precise knowledge of the possible precipitating phases, their crystal chemistry, and their thermodynamic properties. Furthermore, in multicomponent aqueous systems, the precipitation of solid solutions is always a possibility such that the study of arsenate solid solutions involving substitution between atoms of similar size and character is worthwhile [5, 6]. Previous studies indicate that, at high concentrations, compounds in this series could be a limiting phase for arsenic in natural aqueous environments

[7, 8]. In solution, Ba tends to associate with As at pH 7.47–7.66, forming  $\text{BaHAsO}_4\cdot\text{H}_2\text{O}$  and  $\text{Ba}_3(\text{AsO}_4)_2$  [9]. This chemical interaction is used to remove As from aqueous solutions, but its efficiency depends on the solubility of both elements, which is altered by the physicochemical conditions of water [10, 11]. Tiruta-Barna et al. [12] also found that the leaching behaviour of arsenic from a compacted coal fly ash was controlled by the weak soluble phase  $\text{BaHAsO}_4\cdot\text{H}_2\text{O}$ . The only available data on this series correspond to the strontium endmember, whose space group (*Pbca*), cell parameters, and atomic positions of Sr and As were determined by Binns and Boll-Dornberger [13]. From powder diffraction data, Martin et al. [14] determine the same space group for the barium endmember and suggest that  $\text{SrHAsO}_4\cdot\text{H}_2\text{O}$  and  $\text{BaHAsO}_4\cdot\text{H}_2\text{O}$  are isomorphous and therefore good candidates to form solid solutions. The previous data indicate that  $\text{SrHAsO}_4\cdot\text{H}_2\text{O}$  and  $\text{BaHAsO}_4\cdot\text{H}_2\text{O}$  form a complete solid solution where  $\text{Sr}^{2+}$  ions substitute for  $\text{Ba}^{2+}$ . Both endmembers crystallize in the same orthorhombic *Pbca* space group, with lattice parameters that vary significantly with composition [4].

TABLE 1: Summary of synthesis and composition of the  $(\text{Ba}_x\text{Sr}_{1-x})\text{HAsO}_4 \cdot \text{H}_2\text{O}$  solid solution.

Ba(ClO <sub>4</sub> ) <sub>2</sub> 0.5 mol/L	Volumes of the precursors (mL)		Na <sub>3</sub> AsO <sub>4</sub> 0.5 mol/L	Solid solution	
	Sr(ClO <sub>4</sub> ) <sub>2</sub> 0.5 mol/L			Molecular formula	X <sub>Ba</sub>
0	100		100	SrHAsO <sub>4</sub> ·H <sub>2</sub> O	0.00
20	80		100	(Ba <sub>0.21</sub> Sr <sub>0.79</sub> )HAsO <sub>4</sub> ·H <sub>2</sub> O	0.21
40	60		100	(Ba <sub>0.42</sub> Sr <sub>0.58</sub> )HAsO <sub>4</sub> ·H <sub>2</sub> O	0.42
60	40		100	(Ba <sub>0.61</sub> Sr <sub>0.39</sub> )HAsO <sub>4</sub> ·H <sub>2</sub> O	0.61
80	20		100	(Ba <sub>0.82</sub> Sr <sub>0.18</sub> )HAsO <sub>4</sub> ·H <sub>2</sub> O	0.82
100	0		100	BaHAsO <sub>4</sub> ·H <sub>2</sub> O	1.00

The determination of the equilibrium behaviour in SS-AS systems requires knowledge of both the endmember solubility products and the degree of nonideality of the solid solution [5]. Unfortunately, the lack of thermodynamic data for arsenates is even greater than the lack of crystal-chemical data. The  $K_{sp}$  value for BaHAsO<sub>4</sub>·H<sub>2</sub>O was determined to be  $10^{-4.70}$  by Robins [10],  $10^{-24.64}$  by Essington [15],  $10^{-5.31}$  by Itoh and Tozawa [16],  $10^{-0.8}$  by Orellana et al. [17],  $10^{-5.51}$  by Davis [18], and  $10^{-5.60}$  by Zhu et al. [9], which showed a great inconsistency of the currently accepted solubility data. Moreover, the solubility of the strontium endmember as well as the thermodynamic properties of the solid solution is unknown [4]. The fact that there is a significant preferential partitioning of barium toward the solid phase seems to indicate a lesser solubility ( $\approx$  one order of magnitude) for the strontium endmember. A thermodynamic character of these compounds needs to be confirmed [4].

In the present study, a series of the  $(\text{Ba}_x\text{Sr}_{1-x})\text{HAsO}_4 \cdot \text{H}_2\text{O}$  solid solution with different Ba/(Ba + Sr) atomic ratios was prepared by a precipitation method. The resulting solid solution particles were characterized by various techniques. This paper reports the results of a study that monitors the dissolution and release of constituent elements from synthetic  $(\text{Ba}_x\text{Sr}_{1-x})\text{HAsO}_4 \cdot \text{H}_2\text{O}$  solid solutions using batch dissolution experiments. The solid solution aqueous solution reaction paths are also discussed using the Lippmann diagram to evaluate the potential impact of such solid solutions on the mobility of arsenic in the environment.

## 2. Experimental Methods

**2.1. Solid Preparation and Characterization.** The experimental details for the preparation of the samples by precipitation were based on the following equation:  $X^{2+} + \text{HAO}_4^{2-} + \text{H}_2\text{O} = \text{XHAsO}_4 \cdot \text{H}_2\text{O}$ , where  $X = \text{Ba}^{2+}$  or  $\text{Sr}^{2+}$ . The  $(\text{Ba}_x\text{Sr}_{1-x})\text{HAsO}_4 \cdot \text{H}_2\text{O}$  solid solutions were synthesized by controlled mixing of a solution of 100 mL 0.5 M Na<sub>3</sub>AsO<sub>4</sub> and a solution of 100 mL 0.5 M Ba(ClO<sub>4</sub>)<sub>2</sub> and Sr(ClO<sub>4</sub>)<sub>2</sub>, so that the (Ba + Sr)/As molar ratio in the mixed solution was 1.00. The amounts of Ba(ClO<sub>4</sub>)<sub>2</sub> and Sr(ClO<sub>4</sub>)<sub>2</sub> were varied in individual syntheses to obtain synthetic solids with different mole fractions of Ba/(Ba + Sr) (Table 1). Reagent grade chemicals and ultrapure water were used for the synthesis and all experiments. The initial solutions were slowly mixed

in a covered beaker in a course of 10 minutes at room temperature ( $25 \pm 1^\circ\text{C}$ ). The resulting solutions were kept at  $70^\circ\text{C}$  and stirred at a moderate rate (100 rpm) using a stir bar. After one week to crystallize, the precipitates were allowed to settle. The resultant precipitates were then washed thoroughly with ultrapure water and dried for 24 h at  $<110^\circ\text{C}$  to avoid decomposition of the solid samples obtained.

The composition of the solid sample was determined. 50 mg of sample was digested in 10 mL of 2 M HNO<sub>3</sub> solution and then diluted to 50 mL with 2% HNO<sub>3</sub> solution. It was analysed for Ba, Sr, and As using an inductively coupled plasma atomic emission spectrometer (ICP-OES, Perkin Elmer Optima 7000DV). The synthetic solids were also characterised by powder X-ray diffraction (XRD) with an X'Pert PRO diffractometer using Cu K $\alpha$  radiation (40 kV and 40 mA). Crystallographic identification of the synthesised solids was accomplished by comparing the experimental XRD pattern to standard compiled by the International Centre for Diffraction Data (ICDD), which were card 00-023-0823 for BaHAsO<sub>4</sub>·H<sub>2</sub>O and card 01-074-1622 for SrHAsO<sub>4</sub>·H<sub>2</sub>O. The morphology was analysed by scanning electron microscopy (SEM, Joel JSM-6380LV). Infrared transmission spectra (KBr) were recorded over the range of 4000–400 cm<sup>-1</sup> using a Fourier transformed infrared spectrophotometer (FT-IR, Nicolet Nexus 470 FT-IR).

**2.2. Dissolution Experiments.** 1.5 g of the synthetic  $(\text{Ba}_x\text{Sr}_{1-x})\text{HAsO}_4 \cdot \text{H}_2\text{O}$  solid was placed in 250 mL polypropylene bottle. 150 mL of 0.01 M HNO<sub>3</sub> (initial pH 2) was added to each bottle. The bottles were capped and placed in a temperature-controlled water bath ( $25 \pm 1^\circ\text{C}$ ). Water samples (3 mL) were taken from each bottle on 18 occasions (1h, 3h, 6h, 12h, 1d, 2d, 3d, 5d, 10d, 20d, 30d, 40d, 50d, 60d, 75d, 90d, 120d, and 180d). After each sampling, the sample volume was replaced with an equivalent amount of ultrapure water. The samples were filtered using 0.20  $\mu\text{m}$  pore diameter membrane filters and stabilised with 0.2% HNO<sub>3</sub> in 25 mL volumetric flask. Ba, Sr, and As were analysed by using an ICP-OES. After 180 d of dissolution, the solid samples were taken from each bottle, washed, dried, and characterised using XRD, FT-IR, and SEM in the same manner as described above.

**2.3. Thermodynamic Calculations.** Associated with each dissolution is an assemblage of solid phases, a solution phase

containing dissolved calcium, phosphate, arsenate, and a pH value. Assuming equilibrium has been reached, the thermodynamic data can be calculated using established theoretical principles. In this study, the simulations were performed using PHREEQC (Version 3.1.1) together with the most complete literature database minteq.v4.dat, which bases on the ion dissociation theory. The input is free format and uses order-independent keyword data blocks that facilitate the building of models that can simulate a wide variety of aqueous-based scenarios [19]. The aqueous species considered in the calculations were  $\text{Ba}^{2+}$ ,  $\text{BaOH}^+$ ,  $\text{BaAsO}_4^-$ ,  $\text{BaHAsO}_4$ ,  $\text{BaH}_2\text{AsO}_4^+$ ,  $\text{Sr}^{2+}$ ,  $\text{SrOH}^+$ ,  $\text{SrAsO}_4^-$ ,  $\text{SrHAsO}_4$ ,  $\text{SrH}_2\text{AsO}_4^+$ ,  $\text{H}_3\text{AsO}_4$ ,  $\text{H}_2\text{AsO}_4^-$ ,  $\text{HASO}_4^{2-}$ , and  $\text{AsO}_4^{3-}$ . The activities of  $\text{Ba}^{2+}(\text{aq})$ ,  $\text{Sr}^{2+}(\text{aq})$ , and  $\text{HASO}_4^{2-}(\text{aq})$  were firstly calculated by using PHREEQC, and then the ion activity products (IAPs) for  $(\text{Ba}_x\text{Sr}_{1-x})\text{HASO}_4 \cdot \text{H}_2\text{O}$ ,  $\text{BaHAsO}_4 \cdot \text{H}_2\text{O}$ , and  $\text{SrHAsO}_4 \cdot \text{H}_2\text{O}$  were determined according to the mass-action expressions by using Microsoft Excel.

### 3. Results and Discussion

**3.1. Solid Characterizations.** The composition of the synthetic solid depends on the initial Ba: Sr: As mole ratio in the starting solution. To ensure that the  $(\text{Ba}_x\text{Sr}_{1-x})\text{HASO}_4 \cdot \text{H}_2\text{O}$  solid solution was formed, the precipitation was conducted by mixing barium solution, strontium solution, and arsenate solution at low rate. Results suggest that the crystal was the intended composition of  $(\text{Ba}_x\text{Sr}_{1-x})\text{HASO}_4 \cdot \text{H}_2\text{O}$ . The atomic (Ba + Sr)/As ratios were 1.00 which is a stoichiometric ratio of  $(\text{Ba}_x\text{Sr}_{1-x})\text{HASO}_4 \cdot \text{H}_2\text{O}$ . The atomic Ba/(Ba + Sr) ratios ( $X_{\text{Ba}} = 0.00, 0.21, 0.42, 0.61, 0.82, 1.00$ ) were almost the same as those of the precursor solutions ( $x = 0.00, 0.20, 0.40, 0.60, 0.80, 1.00$ ). No  $\text{Na}^+$  and  $\text{NO}_3^-$  were detected in the prepared solid (Table 1).

XRD, FT-IR, and SEM analyses were performed on the solid samples of  $(\text{Ba}_x\text{Sr}_{1-x})\text{HASO}_4 \cdot \text{H}_2\text{O}$  before and after dissolution (Figures 1, 2, and 3). As illustrated in the figures, the results of the analyses on materials before the dissolution were almost indistinguishable from the following reaction. No evidence of secondary mineral precipitation was observed in the dissolution experiment.

The XRD patterns of the obtained solids indicated the formation of the  $(\text{Ba}_x\text{Sr}_{1-x})\text{HASO}_4 \cdot \text{H}_2\text{O}$  solid solution, which has the same type structure as  $\text{BaHAsO}_4 \cdot \text{H}_2\text{O}$  (ICDD PDF 00-023-0823) and  $\text{SrHAsO}_4 \cdot \text{H}_2\text{O}$  (ICDD PDF 01-074-1622) (Figure 1). The patterns correspond exactly with the database patterns and no impurities are observed. The solid solution is complete, with the space group  $\text{Pbca}$  (orthorhombic) being retained throughout.  $\text{BaHAsO}_4 \cdot \text{H}_2\text{O}$  and  $\text{SrHAsO}_4 \cdot \text{H}_2\text{O}$  are the two endmembers of a structural family series. When subjected to XRD, they produce the same reflections; but the reflections exist at different two-theta values; that is, the reflective planes are the same but “ $d$ ” spacings are different. All the compounds have indicated the formation of a solid phase differing only in reflection location, reflection width, and absolute intensity of the diffraction patterns. The reflection peaks of  $\text{BaHAsO}_4 \cdot \text{H}_2\text{O}$  and  $\text{SrHAsO}_4 \cdot \text{H}_2\text{O}$  were slightly different from each other. The reflections of the

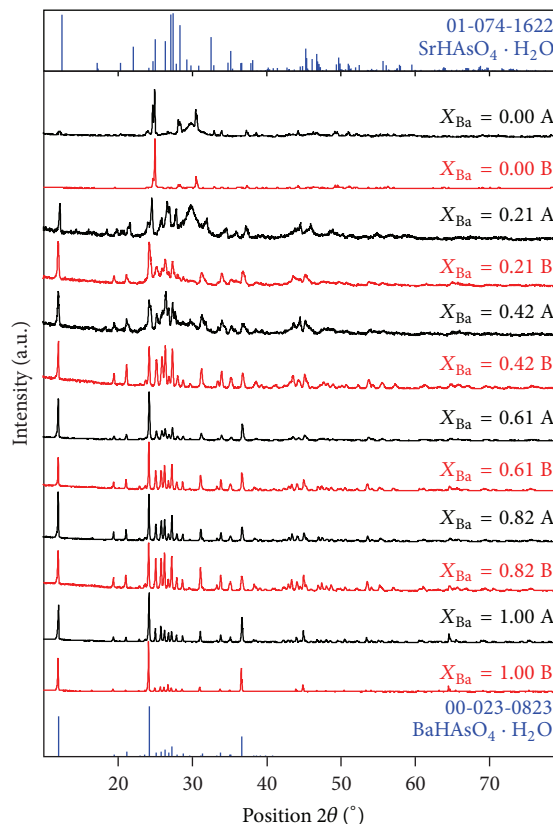


FIGURE 1: XRD patterns of the  $(\text{Ba}_x\text{Sr}_{1-x})\text{HASO}_4 \cdot \text{H}_2\text{O}$  solid solution before (A) and after (B) dissolution.

$(\text{Ba}_x\text{Sr}_{1-x})\text{HASO}_4 \cdot \text{H}_2\text{O}$  solid solutions shifted gradually to a lower-angle direction when the mole fraction  $X_{\text{Ba}}$  of the solids increased (Figure 1).

The FT-IR spectra of the  $(\text{Ba}_x\text{Sr}_{1-x})\text{HASO}_4 \cdot \text{H}_2\text{O}$  solid solutions are shown in Figure 2. The spectra may be divided into three sections: (a) hydroxyl-stretching region, (b) water HOH bending region, and (c) arsenate As–O stretching and OAsO bending region [9]. The free arsenate ion,  $\text{AsO}_4^{3-}$ , belongs to the point group  $T_d$ . The normal modes of the tetrahedral arsenate ion are  $\nu_1$ , symmetric As–O stretching;  $\nu_2$ , OAsO bending;  $\nu_3$ , As–O stretching; and  $\nu_4$ , OAsO bending. In the undistorted state, only the absorptions corresponding to  $\nu_3$  and  $\nu_4$  vibrations are observed. The two remaining fundamentals  $\nu_1$  and  $\nu_2$  become infrared active when the configuration of the  $\text{AsO}_4^{3-}$  ions is reduced to some lower symmetry [9]. The degenerate modes are split by distortion of the arsenate groups through lack of symmetry in the lattice sites. As shown in Figure 2, the bands of  $\text{AsO}_4^{3-}$  appeared around  $815.74, 814.92, \text{ and } 693.82 \text{ cm}^{-1}$  ( $\nu_3$ ) and  $1747.66, 1662.27, 1620.03, \text{ and } 1442.49 \text{ cm}^{-1}$  ( $\nu_1$ ) for the endmember  $\text{BaHAsO}_4 \cdot \text{H}_2\text{O}$  and around  $854.23, 814.92, 704.10 \text{ cm}^{-1}$  ( $\nu_3$ ), and  $1465.20 \text{ cm}^{-1}$  ( $\nu_1$ ) for the endmember  $\text{SrHAsO}_4 \cdot \text{H}_2\text{O}$ . For the  $(\text{Ba}_x\text{Sr}_{1-x})\text{HASO}_4 \cdot \text{H}_2\text{O}$  solid solutions, the  $\nu_1$  and  $\nu_3$  bands shifted slightly to a smaller wavenumber when the mole fraction  $X_{\text{Ba}}$  of the solids increased.

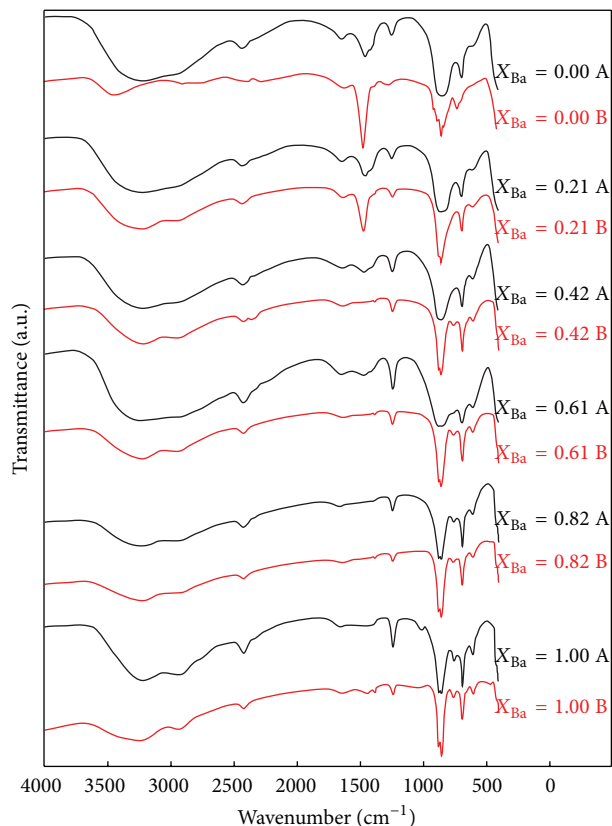


FIGURE 2: FT-IR patterns of the  $(\text{Ba}_x\text{Sr}_{1-x})\text{HAsO}_4\cdot\text{H}_2\text{O}$  solid solution before (A) and after (B) dissolution.

Well-crystallized solids formed (Figure 3). The cell parameters  $a$  and  $b$  and volume increased and  $c$  decreased in a nonlinear way with  $X_{\text{Ba}}$ . The flaky appearance increased; that is, the morphology of the  $(\text{Ba}_x\text{Sr}_{1-x})\text{HAsO}_4\cdot\text{H}_2\text{O}$  solid solutions changed from short prismatic or granular crystals ( $X_{\text{Ba}} = 0$ ) to platy or blades crystals ( $X_{\text{Ba}} = 1$ ).

**3.2. Evolution of Aqueous Composition.** The solution pH and element concentrations during the dissolution experiments at  $25^\circ\text{C}$  and initial pH 2 as a function of time are shown in Figure 4 for the  $(\text{Ba}_x\text{Sr}_{1-x})\text{HAsO}_4\cdot\text{H}_2\text{O}$  solid solution. The experimental results indicated that the dissolution could be stoichiometrical only at the very beginning of the process, and then dissolution became nonstoichiometrical and the system underwent a dissolution-recrystallization process that affects the ratio of the substituting ions in both the solid and the aqueous solution.

When dissolution progressed at the initial pH 2, the aqueous pHs increased rapidly from 2.00 to 5.51–7.71 within the first hour of the experiment. For the dissolution of the  $(\text{Ba}_x\text{Sr}_{1-x})\text{HAsO}_4\cdot\text{H}_2\text{O}$  solid solution with  $X_{\text{Ba}} = 0.00, 0.21, 0.42,$  and  $0.61$ , the solution pHs increased gradually from 1 h to 120 h and after that decreased gradually until they reached the steady state after 2160 h. For the dissolution of the solids with  $X_{\text{Ba}} = 0.82$  and  $1.00$ , the aqueous pHs varied only slightly after 1 h and reached the steady state after 2160 h.

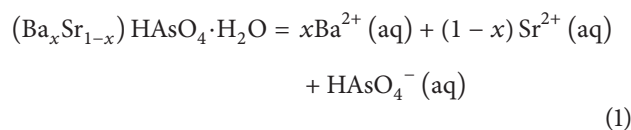
The aqueous pHs decreased with the increasing  $X_{\text{Ba}}$  of the  $(\text{Ba}_x\text{Sr}_{1-x})\text{HAsO}_4\cdot\text{H}_2\text{O}$  solid solution.

For the dissolution of the solids with  $X_{\text{Ba}} = 0.21, 0.42,$  and  $0.61$ , the aqueous Ba concentrations increased rapidly and reached the peak values within the first hour and then decreased gradually and reached the lowest peak values in 240 h. After that, they increased gradually and reached the steady state after 2160 h. For the dissolution of the solids with  $X_{\text{Ba}} = 0.82$  and  $1.00$ , the aqueous Ba concentrations increased rapidly within the first six hours and then increased gradually in 6–480 h. After that, they decreased gradually and reached the steady state after 2160 h. The aqueous Ba concentrations increased with the increasing  $X_{\text{Ba}}$  of the  $(\text{Ba}_x\text{Sr}_{1-x})\text{HAsO}_4\cdot\text{H}_2\text{O}$  solid solution.

When dissolution progressed at the initial pH 2, the aqueous Sr concentrations increased rapidly and reached the peak values within 120–480 h and then decreased gradually until they reached the steady state after 2880 h. The aqueous Sr concentrations increased with the increasing  $X_{\text{Ba}}$  of the  $(\text{Ba}_x\text{Sr}_{1-x})\text{HAsO}_4\cdot\text{H}_2\text{O}$  solid solution with  $0 < X_{\text{Ba}} < 0.21$  (or  $1 < X_{\text{Sr}} < 0.79$ ) and decreased with the increasing  $X_{\text{Ba}}$  of the solids with  $0.21 < X_{\text{Ba}} < 1$  (or  $0.79 < X_{\text{Sr}} < 0$ ); that is, the aqueous Sr concentrations had the highest value for the dissolution of  $(\text{Ba}_{0.21}\text{Sr}_{0.79})\text{HAsO}_4\cdot\text{H}_2\text{O}$ .

The aqueous As(V) concentrations increased rapidly and reached the peak values within the first hour and then decreased gradually and reached the lowest peak values in 48 h. After that, they increased gradually and reached the second peak values in 120–720 h. And then they decreased gradually and reached the steady state after 2880 h. The aqueous As(V) concentrations had the highest value for the dissolution of  $(\text{Ba}_{0.21}\text{Sr}_{0.79})\text{HAsO}_4\cdot\text{H}_2\text{O}$ .

**3.3. Determination of Solubility and Free Energies of Formation.** For the stoichiometric dissolution of the  $(\text{Ba}_x\text{Sr}_{1-x})\text{HAsO}_4\cdot\text{H}_2\text{O}$  solid solution according to



a stoichiometric ion activity product, IAP, can be written as

$$\text{IAP} = \{\text{Ba}^{2+}\}^x \{\text{Sr}^{2+}\}^{(1-x)} \{\text{HAsO}_4^{-}\}. \quad (2)$$

The activities of  $\text{Ba}^{2+}(\text{aq})$ ,  $\text{Sr}^{2+}(\text{aq})$ , and  $\text{HAsO}_4^{2-}(\text{aq})$  were firstly calculated by using PHREEQC [19], and then the IAP values for  $(\text{Ba}_x\text{Sr}_{1-x})\text{HAsO}_4\cdot\text{H}_2\text{O}$ ,  $\text{BaHAsO}_4\cdot\text{H}_2\text{O}$ , and  $\text{SrHAsO}_4\cdot\text{H}_2\text{O}$  were determined according to the mass-action expression (2). The aqueous pH, Ba, Sr, and As concentrations had reached stable values after 2880 h dissolution and the IAP values of 2880 h, 3600 h, and 4320 h were considered as  $K_{\text{sp}}$  of the solids (Figure 4 and Table 2).

For (1),

$$\begin{aligned} \Delta G_r^\circ = & x\Delta G_f^\circ [\text{Ba}^{2+}] + (1-x)\Delta G_f^\circ [\text{Sr}^{2+}] + \Delta G_f^\circ [\text{HAsO}_4^{2-}] \\ & + \Delta G_f^\circ [\text{H}_2\text{O}] - \Delta G_f^\circ [(\text{Ba}_x\text{Sr}_{1-x})\text{HAsO}_4\cdot\text{H}_2\text{O}]. \end{aligned} \quad (3)$$

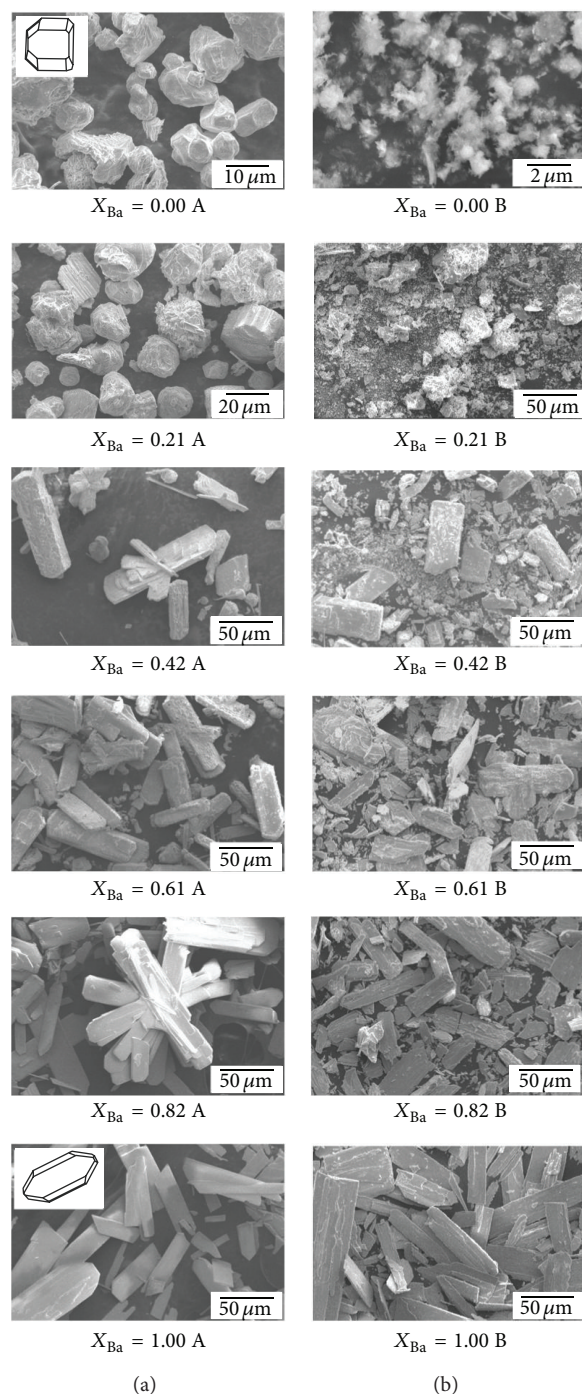


FIGURE 3: SEM images of the  $(\text{Ba}_x\text{Sr}_{1-x})\text{HAsO}_4\cdot\text{H}_2\text{O}$  solid solution before (A) and after (B) dissolution.

Rearranging,

$$\begin{aligned} \Delta G_f^\circ [(\text{Ba}_x\text{Sr}_{1-x})\text{HAsO}_4\cdot\text{H}_2\text{O}] \\ = x\Delta G_f^\circ [\text{Ba}^{2+}] + (1-x)\Delta G_f^\circ [\text{Sr}^{2+}] \\ + \Delta G_f^\circ [\text{HAsO}_4^{2-}] + \Delta G_f^\circ [\text{H}_2\text{O}] - \Delta G_r^\circ. \end{aligned} \quad (4)$$

The standard free energy of reaction ( $\Delta G_r^\circ$ ), in kJ/mol, is related to  $K_{\text{sp}}$  at standard temperature (298.15 K) and pressure (0.101 MPa) by

$$\Delta G_r^\circ = -5.708 \log K_{\text{sp}}. \quad (5)$$

The solution chemistry representing equilibrium involving the solution phase and  $(\text{Ba}_x\text{Sr}_{1-x})\text{HAsO}_4\cdot\text{H}_2\text{O}$ , along with the calculated  $\log K_{\text{sp}}$  using PHREEQC, is shown in Table 2. Based on the obtained literature data,

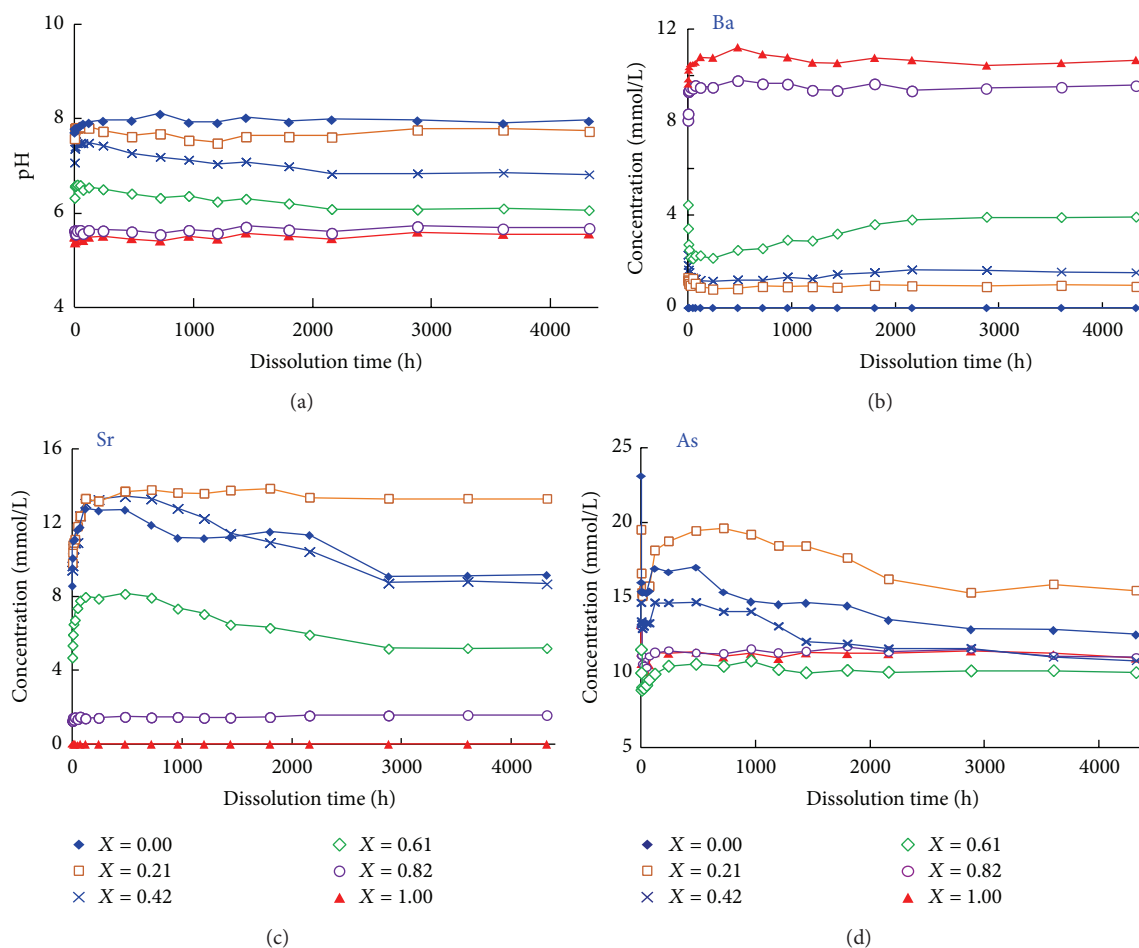


FIGURE 4: Change of the aqueous pH and component concentrations with dissolution time.

$\Delta G_f^\circ[\text{Ba}^{2+}] = -560.77 \text{ kJ/mol}$ ,  $\Delta G_f^\circ[\text{Sr}^{2+}] = -559.84 \text{ kJ/mol}$ ,  $\Delta G_f^\circ[\text{HAsO}_4^{2-}] = -714.59 \text{ kJ/mol}$ ,  $\Delta G_f^\circ[\text{H}_2\text{O}] = -237.141 \text{ kJ/mol}$ , and the free energies of formation,  $\Delta G_f^\circ[(\text{Ba}_x\text{Sr}_{1-x})\text{HAsO}_4 \cdot \text{H}_2\text{O}]$ , were also calculated (Table 2).

The mean  $K_{\text{sp}}$  values were calculated for  $\text{BaHAsO}_4 \cdot \text{H}_2\text{O}$  of  $10^{-5.52}$  ( $10^{-5.49}$ – $10^{-5.53}$ ) at  $25^\circ\text{C}$ , for  $\text{SrHAsO}_4 \cdot \text{H}_2\text{O}$  of  $10^{-4.62}$  at  $25^\circ\text{C}$ . The corresponding free energies of formation ( $\Delta G_f^\circ$ ) were determined to be  $-1543.99 \pm 0.18 \text{ kJ/mol}$  and  $-1537.94 \pm 0.02 \text{ kJ/mol}$ . The  $K_{\text{sp}}$  value of  $10^{-5.52}$  for  $\text{BaHAsO}_4 \cdot \text{H}_2\text{O}$  is approximately 19.12log units higher than  $10^{-24.64}$  reported by Essington [15] and approximately 4.72log units lower than  $10^{-0.8}$  reported by Orellana et al. [17], but in accordance with those of Robins [10], Davis [18], and Zhu et al. [9] ( $10^{-4.70}$ ,  $10^{-5.51}$ , and  $10^{-5.60}$ , resp.). Essington [15] determined the solubility of  $\text{BaHAsO}_4 \cdot \text{H}_2\text{O}(\text{c})$  based not on his own experimental measurement, but on the data of Chukhlantsev [20] for  $\text{Ba}_3(\text{AsO}_4)_2(\text{c})$ . He took the  $\text{Ba}_3(\text{AsO}_4)_2$  solid used by Chukhlantsev [20] for  $\text{BaHAsO}_4 \cdot \text{H}_2\text{O}(\text{c})$  and recalculated the original analytical data. Orellana et al. [17] determined the solubility product only from precipitation experiments. The aqueous solution in his experiment might not reach equilibrium and was still supersaturated with regard to the

solid. Based on our experimental results and those available in the literature, the solubility product for  $\text{BaHAsO}_4 \cdot \text{H}_2\text{O}$  should be around  $10^{-5.50}$ .

$\text{BaHAsO}_4 \cdot \text{H}_2\text{O}$  is less soluble than  $\text{SrHAsO}_4 \cdot \text{H}_2\text{O}$ . For the  $(\text{Ba}_x\text{Sr}_{1-x})\text{HAsO}_4 \cdot \text{H}_2\text{O}$  solid solution, the solubility decreased as  $X_{\text{Ba}}$  increased when  $0.00 < X_{\text{Ba}} < 0.82$  and increased as  $X_{\text{Ba}}$  increased when  $0.82 < X_{\text{Ba}} < 1.00$ . The  $(\text{Ba}_x\text{Sr}_{1-x})\text{HAsO}_4 \cdot \text{H}_2\text{O}$  solid solution had a minimum solubility product of  $10^{-5.61}$  at  $X_{\text{Ba}} = 0.82$ . This variation tendency is in accordance with the change of the unit cell parameters [4].

**3.4. Saturation Index for  $\text{BaHAsO}_4 \cdot \text{H}_2\text{O}$  and  $\text{SrHAsO}_4 \cdot \text{H}_2\text{O}$ .**  
 The  $K_{\text{sp}}$  values of  $10^{-5.52}$  for  $\text{BaHAsO}_4 \cdot \text{H}_2\text{O}$  and  $10^{-4.62}$  for  $\text{SrHAsO}_4 \cdot \text{H}_2\text{O}$  were used in the calculation using the program PHREEQC in the present study. The calculated saturation indices for  $\text{BaHAsO}_4 \cdot \text{H}_2\text{O}$  show a trend of increasing values as the composition of the solid phases approaches that of the pure-phase endmember,  $\text{BaHAsO}_4 \cdot \text{H}_2\text{O}$  (Figure 5). At the beginning of the dissolution of the  $(\text{Ba}_x\text{Sr}_{1-x})\text{HAsO}_4 \cdot \text{H}_2\text{O}$  solid solution, the  $\text{BaHAsO}_4 \cdot \text{H}_2\text{O}$  saturated index (SI) values increased with

TABLE 2: Analytical data and solubility determination of the  $(\text{Ba}_x\text{Sr}_{1-x})\text{HAsO}_4 \cdot \text{H}_2\text{O}$  solid solution.

Sample	Dissolution time (h)	pH	Concentration (mmol/L)			$\log K_{\text{sp}}$	Average $\log K_{\text{sp}}$	$\Delta G_f^\circ$ (kJ/mol)
			Ba	Sr	As			
$\text{SrHAsO}_4 \cdot \text{H}_2\text{O}$	2880	7.96	0.00	9.08	12.88	-4.62	-4.62	-1537.94
	3600	7.90	0.00	9.12	12.83	-4.62		
	4320	7.95	0.00	9.16	12.53	-4.62		
$(\text{Ba}_{0.21}\text{Sr}_{0.79})\text{HAsO}_4 \cdot \text{H}_2\text{O}$	2880	7.77	0.91	13.34	15.38	-4.70	-4.69	-1538.54
	3600	7.77	0.98	13.32	15.54	-4.69		
	4320	7.74	0.94	13.32	15.53	-4.69		
$(\text{Ba}_{0.42}\text{Sr}_{0.58})\text{HAsO}_4 \cdot \text{H}_2\text{O}$	2880	6.86	1.63	8.73	11.68	-5.11	-5.13	-1541.25
	3600	6.85	1.56	8.82	11.07	-5.13		
	4320	6.83	1.54	8.69	10.81	-5.15		
$(\text{Ba}_{0.61}\text{Sr}_{0.39})\text{HAsO}_4 \cdot \text{H}_2\text{O}$	2880	6.18	3.92	5.18	10.15	-5.45	-5.49	-1543.50
	3600	6.10	3.91	5.17	10.17	-5.51		
	4320	6.06	3.93	5.20	10.24	-5.53		
$(\text{Ba}_{0.82}\text{Sr}_{0.18})\text{HAsO}_4 \cdot \text{H}_2\text{O}$	2880	5.72	9.45	1.55	11.58	-5.57	-5.61	-1544.24
	3600	5.67	9.51	1.56	11.16	-5.63		
	4320	5.68	9.57	1.57	11.07	-5.62		
$\text{BaHAsO}_4 \cdot \text{H}_2\text{O}$	2880	5.61	10.53	0.00	11.42	-5.49	-5.52	-1543.99
	3600	5.56	10.56	0.00	11.25	-5.53		
	4320	5.57	10.69	0.00	10.94	-5.53		

time until the aqueous solution was oversaturated with respect to  $\text{BaHAsO}_4 \cdot \text{H}_2\text{O}$ , and then the SI values decreased slowly. At the end of the dissolution experiment (2880–4320 h), the aqueous solution was saturated with respect to  $\text{BaHAsO}_4 \cdot \text{H}_2\text{O}$  for the  $(\text{Ba}_x\text{Sr}_{1-x})\text{HAsO}_4 \cdot \text{H}_2\text{O}$  solid solution with  $\text{SI} = -0.06 \sim 0.10$ .

The calculated saturation indices for  $\text{SrHAsO}_4 \cdot \text{H}_2\text{O}$  show a distinctly different trend than those for  $\text{BaHAsO}_4 \cdot \text{H}_2\text{O}$  (Figure 5). For the  $(\text{Ba}_x\text{Sr}_{1-x})\text{HAsO}_4 \cdot \text{H}_2\text{O}$  solid solution with  $x > 0.2$ , the  $\text{SrHAsO}_4 \cdot \text{H}_2\text{O}$  saturated index (SI) values decreased as the  $\text{SrHAsO}_4 \cdot \text{H}_2\text{O}$  mole fraction decreased or the  $\text{BaHAsO}_4 \cdot \text{H}_2\text{O}$  mole fraction increased for the  $(\text{Ba}_x\text{Sr}_{1-x})\text{HAsO}_4 \cdot \text{H}_2\text{O}$  solid solution with  $x > 0.2$ . The  $\text{SrHAsO}_4 \cdot \text{H}_2\text{O}$  saturated index (SI) values increased with time for the  $(\text{Ba}_x\text{Sr}_{1-x})\text{HAsO}_4 \cdot \text{H}_2\text{O}$  solid solution with  $x > 0.2$ . For the  $(\text{Ba}_x\text{Sr}_{1-x})\text{HAsO}_4 \cdot \text{H}_2\text{O}$  solid solution with  $x \leq 0.2$ , the  $\text{SrHAsO}_4 \cdot \text{H}_2\text{O}$  saturated index (SI) values increased as the  $\text{SrHAsO}_4 \cdot \text{H}_2\text{O}$  mole fraction increased or the  $\text{BaHAsO}_4 \cdot \text{H}_2\text{O}$  mole fraction decreased for the  $(\text{Ba}_x\text{Sr}_{1-x})\text{HAsO}_4 \cdot \text{H}_2\text{O}$  solid solution with  $x \leq 0.2$ . At the beginning of the dissolution, the  $\text{SrHAsO}_4 \cdot \text{H}_2\text{O}$  saturated index (SI) values increased with time until the aqueous solution was oversaturated with respect to  $\text{SrHAsO}_4 \cdot \text{H}_2\text{O}$ , and then the SI values decreased slowly. At the end of the dissolution experiment (4320 h), the aqueous solution was saturated with respect to  $\text{SrHAsO}_4 \cdot \text{H}_2\text{O}$  for the  $(\text{Ba}_x\text{Sr}_{1-x})\text{HAsO}_4 \cdot \text{H}_2\text{O}$  solid solution with  $x \leq 0.2$ , while the aqueous solution was undersaturated with respect to  $\text{SrHAsO}_4 \cdot \text{H}_2\text{O}$  for the  $(\text{Ba}_x\text{Sr}_{1-x})\text{HAsO}_4 \cdot \text{H}_2\text{O}$  solid solution with  $x > 0.2$ .

### 3.5. Lippmann Diagram

3.5.1. Construction of Lippmann Diagram. Understanding solid solution aqueous solution (SSAS) processes is of

fundamental importance. However, in spite of the numerous studies, the availability of thermodynamic data for SSAS systems is still scarce [6]. Lippmann extended the solubility product concept to solid solutions by developing the concept of “total solubility product  $\Sigma\Pi_{\text{SS}}$ ” which is defined as the sum of the partial activity products contributed by the individual endmembers of the solid solution [5, 6]. At thermodynamic equilibrium, the total activity product  $\Sigma\Pi_{\text{SS}}$ , expressed as a function of the solid composition, yields Lippmann’s “*solidus*” relationship. In the same way, the “*solutus*” relationship expresses  $\Sigma\Pi_{\text{SS}}$  as a function of the aqueous solution composition. The graphical representation of “*solidus*” and “*solutus*” yields a phase diagram, usually known as a Lippmann diagram [5, 6]. A comprehensive methodology for describing reaction paths and equilibrium end points in solid solution aqueous solution systems had been presented and discussed in literatures [5, 6, 21–23].

In the case of the  $(\text{Ba}_x\text{Sr}_{1-x})\text{HAsO}_4 \cdot \text{H}_2\text{O}$  solid solution, the term “total solubility product  $\Sigma\Pi_{\text{SS}}$ ” is defined as the  $(\{\text{Ba}^{2+}\} + \{\text{Sr}^{2+}\})\{\text{HAsO}_4^{2-}\}$  at equilibrium and can be expressed by

$$\Sigma\Pi_{\text{SS}} = K_{\text{Ba}}X_{\text{Ba}}\gamma_{\text{Ba}} + K_{\text{Sr}}X_{\text{Sr}}\gamma_{\text{Sr}}, \quad (6)$$

where  $\{\}$  designate aqueous activity,  $K_{\text{Ba}}$  and  $K_{\text{Sr}}$ ,  $X_{\text{Ba}}$  and  $X_{\text{Sr}}$ , and  $\gamma_{\text{Ba}}$  and  $\gamma_{\text{Sr}}$  are the thermodynamic solubility products, the mole fractions ( $x, 1-x$ ), and the activity coefficients of the  $\text{BaHAsO}_4 \cdot \text{H}_2\text{O}$  and  $\text{SrHAsO}_4 \cdot \text{H}_2\text{O}$  components in the  $(\text{Ba}_x\text{Sr}_{1-x})\text{HAsO}_4 \cdot \text{H}_2\text{O}$  solid solution, respectively. This relationship, called the *solidus*, defines all possible thermodynamic saturation states for the two-component solid solution series in terms of the solid phase composition.

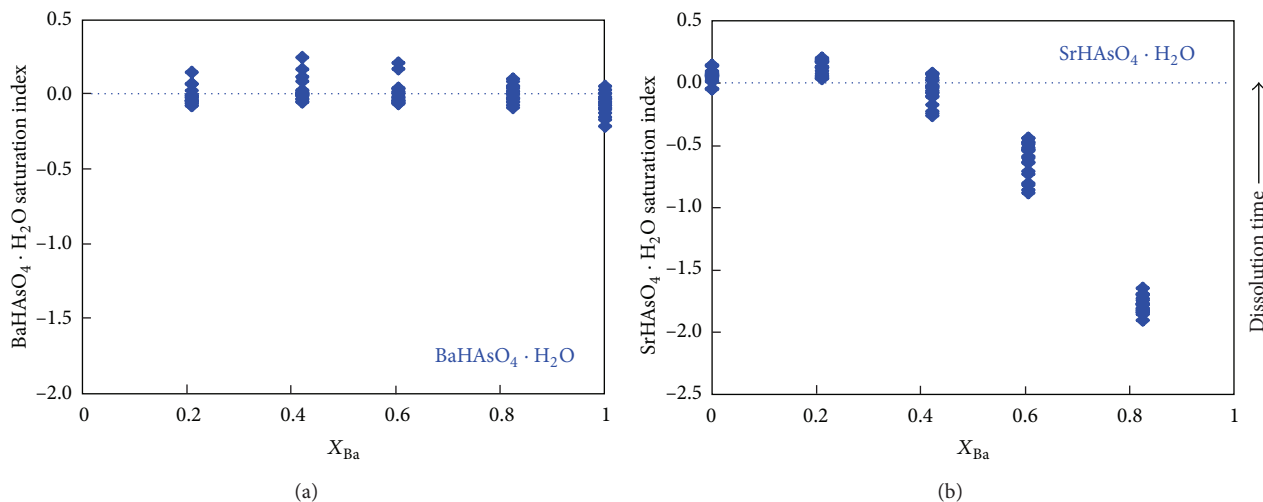


FIGURE 5: Saturation indices for BaHAsO<sub>4</sub>·H<sub>2</sub>O and SrHAsO<sub>4</sub>·H<sub>2</sub>O.

The term “total solubility product  $\Sigma\Pi_{SS}$ ” can also be expressed by

$$\Sigma\Pi_{SS} = \frac{1}{X_{Ba^{2+},aq}/K_{Ba}\gamma_{Ba} + X_{Sr^{2+},aq}/K_{Sr}\gamma_{Sr}}, \quad (7)$$

where  $X_{Ba^{2+},aq}$  and  $X_{Sr^{2+},aq}$  are the activity fractions of the aqueous Ba and Sr components. This relationship, called the *solutus*, defines all possible thermodynamic saturation states for the two-component solid solution series in terms of the aqueous phase composition.

For a solid solution with fixed composition  $X_{Ba} = 1 - X_{Sr}$ , a series of minimum stoichiometric saturation scenarios as a function of the aqueous activity fraction  $X_{Ba^{2+},aq}$  of the substituting ions in the aqueous solution can be described by

$$\Sigma\Pi_{SS} = \frac{IAP}{(X_{Ba^{2+},aq})^{x_{Ba}}(X_{Sr^{2+},aq})^{x_{Sr}}}. \quad (8)$$

For the endmembers BaHAsO<sub>4</sub>·H<sub>2</sub>O and SrHAsO<sub>4</sub>·H<sub>2</sub>O and  $X_{Ba} = 1$  and  $X_{Sr} = 0$ , the endmember saturation equations can be written as

$$\begin{aligned} \Sigma\Pi_{BaHAsO_4 \cdot H_2O} &= \frac{\{Ba^{2+}\}\{HAsO_4^{2-}\}}{(X_{Ba^{2+},aq})^{x_{Ba}}} = \frac{K_{Ba}}{(X_{Ba^{2+},aq})^{x_{Ba}}}, \\ \Sigma\Pi_{SrHAsO_4 \cdot H_2O} &= \frac{\{Sr^{2+}\}\{HAsO_4^{2-}\}}{(X_{Sr^{2+},aq})^{x_{Sr}}} = \frac{K_{Sr}}{(X_{Sr^{2+},aq})^{x_{Sr}}}. \end{aligned} \quad (9)$$

A Lippmann phase diagram for the  $(Ba_xSr_{1-x})HAsO_4 \cdot H_2O$  solid solution is a plot of the *solidus* and *solutus* as  $\log \Sigma\Pi_{SS}$  on the ordinate versus two superimposed aqueous and solid phase mole fraction scales on the abscissa.

**3.5.2. Lippmann Diagram for the Ideal Solid Solution.** In the  $(Ba_xSr_{1-x})HAsO_4 \cdot H_2O$  system, the endmember solubility products are  $-5.52$  for BaHAsO<sub>4</sub>·H<sub>2</sub>O and  $-4.62$  for SrHAsO<sub>4</sub>·H<sub>2</sub>O; that is, they differ by about 0.9 log units. The

$(Ba_xSr_{1-x})HAsO_4 \cdot H_2O$  solid solutions are assumed ideal. In this case, the pure-phase solubility curves for BaHAsO<sub>4</sub>·H<sub>2</sub>O and SrHAsO<sub>4</sub>·H<sub>2</sub>O are quite distinct from the *solutus*, and the solution compositions along the *solutus* are clearly undersaturated with respect to both pure BaHAsO<sub>4</sub>·H<sub>2</sub>O and SrHAsO<sub>4</sub>·H<sub>2</sub>O solids. The dotted horizontal tie lines indicate the relation between the solid mole fractions and the aqueous activity fractions at thermodynamic equilibrium (points T2 and T1) or at primary saturation (points P2 and P1) with respect to a  $(Ba_{0.61}Sr_{0.39})HAsO_4 \cdot H_2O$  solid. The dashed curve gives the series of possible  $(X_{Ba^{2+},aq}, \Sigma\Pi_{SS})$  aqueous compositions that satisfy the condition of stoichiometric saturation with respect to a  $(Ba_{0.61}Sr_{0.39})HAsO_4 \cdot H_2O$  solid. Point M1 is the “minimum stoichiometric saturation” point for a  $(Ba_{0.61}Sr_{0.39})HAsO_4 \cdot H_2O$  solid.

As with all the “minimum stoichiometric saturation” curves, the “pure endmember saturation” curves plot above the *solutus* for all aqueous activity fractions, concurring with the *solutus* only for  $X_{Ba^{2+},aq}$  or  $X_{Sr^{2+},aq}$  equal to one. This can be seen in Figure 6, in which the curves  $\Sigma\Pi_{BaHAsO_4 \cdot H_2O}$  and  $\Sigma\Pi_{SrHAsO_4 \cdot H_2O}$  have been represented for the same solid solution as in Figure 6. Note that the two curves intersect at the point “S.” This point represents an aqueous solution at simultaneous stoichiometric saturation with respect to both endmembers.

The hypothetical reaction path is also shown in Figure 6, in relation to Lippmann *solutus* and *solidus* curves for the  $(Ba_{0.61}Sr_{0.39})HAsO_4 \cdot H_2O$  solid solution. The reaction path of a stoichiometrically dissolving solid solution moves vertically from the abscissa of a Lippmann diagram, originating at the mole fraction corresponding to the initial solid solution composition. The pathway shows initial stoichiometric dissolution up to the *solutus* curve, followed by nonstoichiometric dissolution along the *solutus*, towards the more soluble endmember.

The difference between the solubility products of the endmembers involves a strong preferential partitioning of the less soluble endmember towards the solid phase. Our dissolution data indicate a final enrichment in the BaHAsO<sub>4</sub>·H<sub>2</sub>O

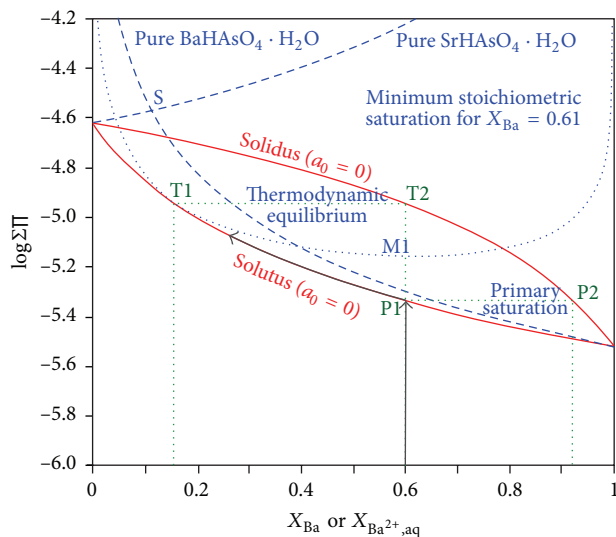


FIGURE 6: Lippmann diagram for the  $(\text{Ba}_x\text{Sr}_{1-x})\text{HASO}_4\cdot\text{H}_2\text{O}$  ideal solid solution.

component in the solid phase and a persistent enrichment in the  $\text{Sr}^{2+}$  component in the aqueous phase. The possibility of formation of a phase close in composition to pure  $\text{BaHASO}_4\cdot\text{H}_2\text{O}$  seems unavoidable, given the lower solubility of  $\text{BaHASO}_4\cdot\text{H}_2\text{O}$  and the oversaturation with respect to  $\text{BaHASO}_4\cdot\text{H}_2\text{O}$  and the relatively high solubility of  $\text{SrHASO}_4\cdot\text{H}_2\text{O}$  and the undersaturation with respect to  $\text{SrHASO}_4\cdot\text{H}_2\text{O}$  (Figure 5). From the point of view of the crystallization behavior, all data seem to indicate that there is a preferential partitioning of barium into the solid phase [4].

**3.5.3. Lippmann Diagram for the Nonideal Solid Solution.** Complementary powder XRD measurements indicated that the cell parameters increased in a nonlinear way with  $X_{\text{Ba}}$  indicating the solid solution is complete but could be nonideal [4]. The solid phase activity coefficients of  $\text{BaHASO}_4\cdot\text{H}_2\text{O}$  ( $\gamma_{\text{Ba}}$ ) and  $\text{SrHASO}_4\cdot\text{H}_2\text{O}$  ( $\gamma_{\text{Sr}}$ ) as components of the solid solution can be calculated as a function of composition using the Redlich and Kister equations [5, 6], expressed in the form

$$\begin{aligned} \ln \gamma_{\text{Ba}} &= (1-x)^2 [a_0 - a_1 (3x - (1-x)) + \dots], \\ \ln \gamma_{\text{Sr}} &= x^2 [a_0 - a_1 (3(1-x) - x) + \dots], \end{aligned} \quad (10)$$

where  $x$  and  $1-x$  are the mole fractions ( $X_{\text{Ba}}$  and  $X_{\text{Sr}}$ ) of the  $\text{BaHASO}_4\cdot\text{H}_2\text{O}$  and  $\text{SrHASO}_4\cdot\text{H}_2\text{O}$  components in the  $(\text{Ba}_x\text{Sr}_{1-x})\text{HASO}_4\cdot\text{H}_2\text{O}$  solid solution; the Guggenheim coefficients  $a_0$  and  $a_1$  can be determined from an expansion of the excess Gibbs free energy of mixing  $G^E$  [5, 6].

The excess Gibbs free energy of mixing  $G^E$  has not been measured for the  $(\text{Ba}_x\text{Sr}_{1-x})\text{HASO}_4\cdot\text{H}_2\text{O}$  solid solution. Assuming that a stoichiometric saturation state was attained

in the dissolution experiments, the Guggenheim coefficients  $a_0$  and  $a_1$  can be estimated from

$$\begin{aligned} \ln K_{\text{sp}} &= x(1-x)a_0 + x(1-x)(x-(1-x))a_1 \\ &+ (1-x) \ln [(1-x)K_{\text{Ba}}] + x \ln [xK_{\text{Sr}}]. \end{aligned} \quad (11)$$

Log IAP ( $\log K_{\text{sp}}$ ) values of the samples taken after 2880 h dissolution are shown as a function of  $X_{\text{Ba}}$  in Figure 7. A plot of these  $\log K_{\text{sp}}$  values versus solid mole fraction of  $\text{BaHASO}_4\cdot\text{H}_2\text{O}$  shows that the  $\log K_{\text{sp}}$  values are close to and slightly lower than what would be expected for an ideal solid solution. Fitting the  $K_{\text{sp}}$  values as a function of solid composition to (11) yields a best fit with a two-parameter Guggenheim model of  $a_0 = 1.55$  and  $a_1 = -4.35$  ( $R^2 > 0.95$ ) (Figure 7).

The diagram of Figure 8 is a typical Lippmann diagram for a solid solution with a negative enthalpy of mixing. The negative excess free energy of mixing produces a fall of the *solutus* curve with respect to the position of an equivalent ideal *solutus*. This means that the solubility of intermediate compositions is significantly smaller than that of an equivalent ideal solid solution. Indeed, for a certain range of solid compositions, the *solutus* values plot below the solubility product of the less soluble endmember. The system shows an ‘‘alotropic’’ minimum at  $X_{\text{Ba}^{2+},\text{aq}} = 0.87$  where the *solutus* and *solidus* curves meet. Such a point represents a thermodynamic equilibrium state in which the mole fraction of the substituting ions in the solid phase equals its activity fraction in the aqueous solution. Obviously, at the alotropic point, the equilibrium distribution coefficient is equal to unity [5, 6].

**3.5.4. Solid Solution Aqueous Solution Reaction Paths.** A Lippmann diagram for the  $(\text{Ba}_x\text{Sr}_{1-x})\text{HASO}_4\cdot\text{H}_2\text{O}$  solid solution for the ideal case when  $a_0 = 0.0$  is shown in Figure 9. In addition to the *solutus* and the *solidus*, the diagrams contain the total solubility product curve at stoichiometric saturation for the  $(\text{Ba}_x\text{Sr}_{1-x})\text{HASO}_4\cdot\text{H}_2\text{O}$  solid solution at  $x = 0.21, 0.42, 0.61,$  and  $0.82$ . The saturation curves for pure endmembers  $\text{BaHASO}_4\cdot\text{H}_2\text{O}$  ( $x = 1.00$ ) and  $\text{SrHASO}_4\cdot\text{H}_2\text{O}$  ( $x = 0.00$ ) have also been plotted in the chart. Also included are the data from our study, plotted as  $(\{\text{Ba}^{2+}\} + \{\text{Sr}^{2+}\})\{\text{HASO}_4^{2-}\}$  versus  $X_{\text{Ba}^{2+},\text{aq}}$ .

In general, the location of data points on a Lippmann diagram will depend on the aqueous speciation, degree to which secondary phases are formed, and the relative rates of dissolution and precipitation. As  $(\text{Ba}_x\text{Sr}_{1-x})\text{HASO}_4\cdot\text{H}_2\text{O}$  dissolves in solution, aqueous  $\text{Ba}^{2+}$  is converted into  $\text{Ba}^{2+}$ ,  $\text{BaOH}^+$ ,  $\text{BaAsO}_4^-$ ,  $\text{BaHASO}_4$ , and  $\text{BaH}_2\text{AsO}_4^+$ , and aqueous  $\text{Sr}^{2+}$  is converted into  $\text{Sr}^{2+}$ ,  $\text{SrOH}^+$ ,  $\text{SrAsO}_4^-$ ,  $\text{SrHASO}_4$ , and  $\text{SrH}_2\text{AsO}_4^+$ ; aqueous  $\text{HASO}_4^{2-}$  is converted primarily into  $\text{AsO}_4^{3-}$ ,  $\text{H}_2\text{AsO}_4^-$ , and  $\text{H}_3\text{AsO}_4$  and only a fraction remains as  $\text{Ba}^{2+}$ ,  $\text{Sr}^{2+}$ , and  $\text{HASO}_4^{2-}$ . The smaller values of the activity fractions are a consequence of the  $\text{Ba}^{2+}$  and  $\text{Sr}^{2+}$  speciation. For the plot of the experimental data on the Lippmann diagram, the effect of the aqueous  $\text{Ba}^{2+}$  and  $\text{Sr}^{2+}$  speciation was considered by calculating the activity of  $\text{Ba}^{2+}$  and  $\text{Sr}^{2+}$  with the program PHREEQC.

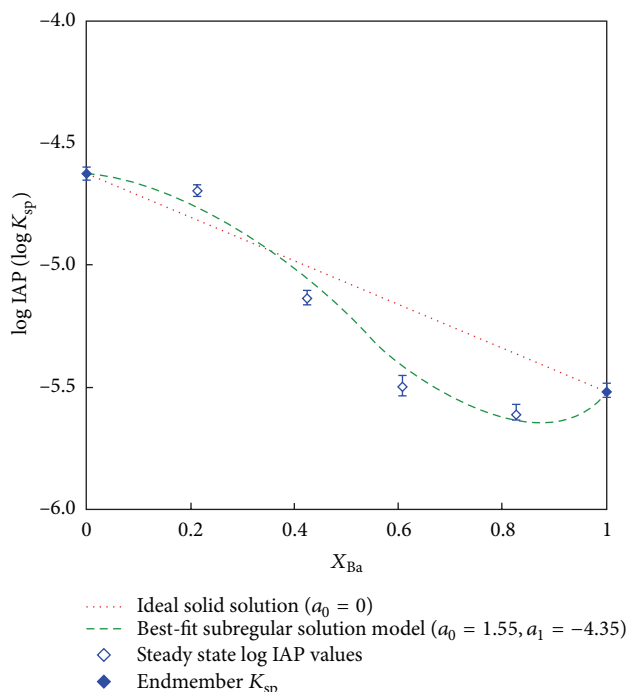


FIGURE 7: Estimation of the Guggenheim coefficients for the  $(\text{Ba}_x\text{Sr}_{1-x})\text{HASO}_4 \cdot \text{H}_2\text{O}$  nonideal solid solution.

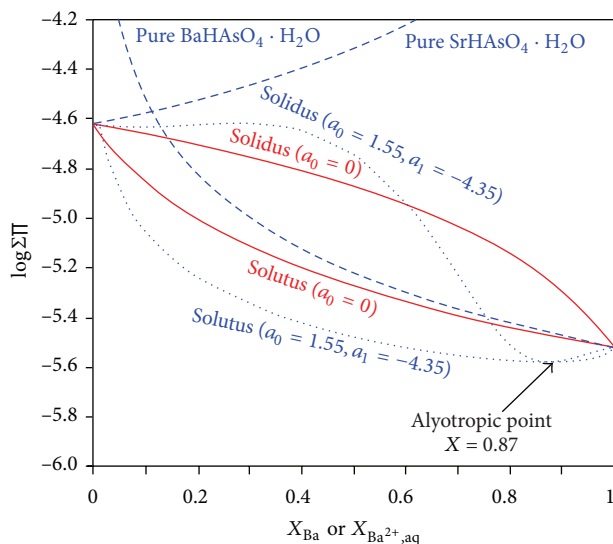


FIGURE 8: Lippmann diagram for the  $(\text{Ba}_x\text{Sr}_{1-x})\text{HASO}_4 \cdot \text{H}_2\text{O}$  nonideal solid solution.

The experimental data plotted on Lippmann phase diagrams show that the  $(\text{Ba}_{0.61}\text{Sr}_{0.39})\text{HASO}_4 \cdot \text{H}_2\text{O}$  precipitate dissolved stoichiometrically at the beginning and approached the Lippmann *solutus* curve and then overshot the Lippmann *solutus* curve, the saturation curves for pure endmembers  $\text{BaHASO}_4 \cdot \text{H}_2\text{O}$ , and the stoichiometric saturation curve for  $x = 0.61$ . After about 1 h dissolution, the aqueous solution was oversaturated with respect to  $\text{BaHASO}_4 \cdot \text{H}_2\text{O}$  and the  $(\text{Ba}_x\text{Sr}_{1-x})\text{HASO}_4 \cdot \text{H}_2\text{O}$  solid solution. And then, the  $X_{\text{Ba}^{2+},\text{aq}}$

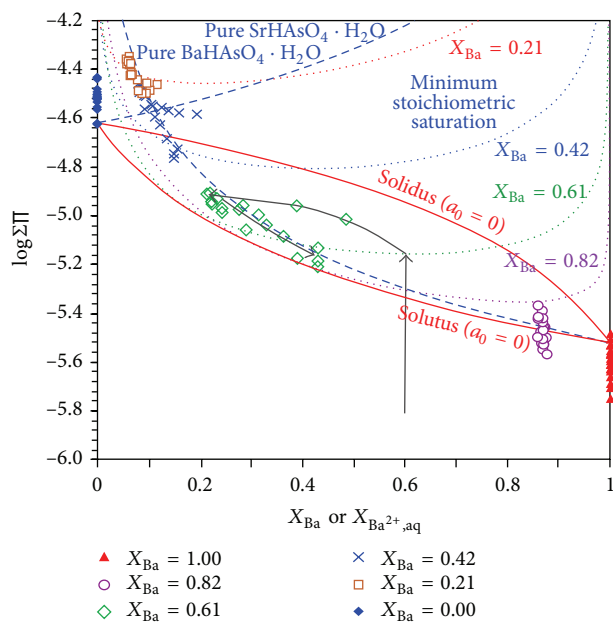


FIGURE 9: Plot of the experimental data on the Lippmann diagram.

decreased from 0.61 to 0.21 in 240 h with no obvious change in the  $\log \Sigma \Pi_{\text{SS}}$  value, indicating the dissolution path for this precipitate may involve stoichiometric dissolution to the Lippmann *solutus* curve and overshot the Lippmann *solutus* curve followed by a possible exchange and recrystallization reaction. From 240 to 4320 h, the  $\log \Sigma \Pi_{\text{SS}}$  value decreased further, but the  $X_{\text{Ba}^{2+},\text{aq}}$  increased from 0.21 to about 0.43, and the dissolution followed the saturation curve for pure endmembers  $\text{BaHASO}_4 \cdot \text{H}_2\text{O}$  and approached the intersection with the minimum stoichiometric saturation curve for  $x = 0.61$ .

#### 4. Conclusions

With the increasing  $X_{\text{Ba}}$ , the morphology of the  $(\text{Ba}_x\text{Sr}_{1-x})\text{HASO}_4 \cdot \text{H}_2\text{O}$  solid solutions changed from short prismatic or granular crystals ( $X_{\text{Ba}} = 0$ ) to platy or blades crystals ( $X_{\text{Ba}} = 1$ ). The synthetic solids used in the experiments were found to have no obvious variation after dissolution. During the dissolution of the solid solution, the aqueous pH values and component concentrations increased rapidly at the beginning and then varied slowly with time and finally exhibited stable state after 2880 h dissolution. With the increasing  $X_{\text{Ba}}$ , the aqueous pH value decreased and the aqueous Ba concentration increased. At  $X_{\text{Ba}} = 0.21$ , the aqueous Sr and As concentrations had the highest values. The solubility products ( $K_{\text{sp}}$ ) for  $\text{BaHASO}_4 \cdot \text{H}_2\text{O}$  and  $\text{SrHASO}_4 \cdot \text{H}_2\text{O}$  were calculated to be  $10^{-5.52}$  and  $10^{-4.62}$ , respectively. The corresponding free energies of formation ( $\Delta G_f^\circ$ ) were  $-1543.99 \pm 0.18$  kJ/mol and  $-1537.94 \pm 0.02$  kJ/mol.  $\text{BaHASO}_4 \cdot \text{H}_2\text{O}$  is less soluble than  $\text{SrHASO}_4 \cdot \text{H}_2\text{O}$ . For the  $(\text{Ba}_x\text{Sr}_{1-x})\text{HASO}_4 \cdot \text{H}_2\text{O}$  solid solution, the solubility decreased as  $X_{\text{Ba}}$  increased when  $0.00 < X_{\text{Ba}} < 0.82$  and increased as  $X_{\text{Ba}}$  increased when

$0.82 < X_{\text{Ba}} < 1.00$ . The  $(\text{Ba}_x\text{Sr}_{1-x})\text{HAsO}_4 \cdot \text{H}_2\text{O}$  solid solution had a minimum solubility product of  $10^{-5.61}$  at  $X_{\text{Ba}} = 0.82$ . The Guggenheim coefficients were determined to be  $a_0 = 1.55$  and  $a_1 = -4.35$  for the  $(\text{Ba}_x\text{Sr}_{1-x})\text{HAsO}_4 \cdot \text{H}_2\text{O}$  nonideal solid solution. The constructed Lippmann diagram was a typical Lippmann diagram for a nonideal solid solution with a negative enthalpy of mixing, which produced a fall of the *solutus* curve with respect to the position of an equivalent ideal *solutus*, which indicated that the solubility of intermediate compositions is significantly smaller than that of an equivalent ideal solid solution. The system shows an “alloyotropic” minimum at  $X_{\text{Ba}^{2+},\text{aq}} = 0.87$ . At the end of the experiment, the dissolution followed the saturation curve for the pure endmember  $\text{BaHAsO}_4 \cdot \text{H}_2\text{O}$  and approached the intersection with the minimum stoichiometric saturation curve on the Lippmann diagram.

### Conflict of Interests

The authors declare that there is no conflict of interests regarding the publication of this paper.

### Acknowledgments

The authors thank the financial supports from the National Natural Science Foundation of China (41263009, 40773059) and the Provincial Natural Science Foundation of Guangxi (2012GXNSFDA053022, 2011GXNSFF018003).

### References

- [1] E. Fulladosa, J. C. Murat, M. Martínez, and I. Villaescusa, “Effect of pH on arsenate and arsenite toxicity to luminescent bacteria (*vibrio fischeri*),” *Archives of Environmental Contamination and Toxicology*, vol. 46, no. 2, pp. 176–182, 2004.
- [2] D. Mohan and C. U. Pittman Jr., “Arsenic removal from water/wastewater using adsorbents—a critical review,” *Journal of Hazardous Materials*, vol. 142, no. 1–2, pp. 1–53, 2007.
- [3] P. L. Smedley and D. G. Kinniburgh, “A review of the source, behaviour and distribution of arsenic in natural waters,” *Applied Geochemistry*, vol. 17, no. 5, pp. 517–568, 2002.
- [4] A. Jiménez, M. Prieto, Salvador M. A., and S. García-Granda, “Structure and crystallization behavior of the  $(\text{Ba},\text{Sr})\text{HAsO}_4 \cdot \text{H}_2\text{O}$  solid-solution in aqueous environments,” *American Mineralogist*, vol. 89, pp. 601–609, 2004.
- [5] P. D. Glynn and E. J. Reardon, “Solid-solution aqueous-solution equilibria: thermodynamic theory and representation,” *American Journal of Science*, vol. 290, no. 2, pp. 164–201, 1990.
- [6] M. Prieto, “Thermodynamics of solid solution aqueous solution systems,” *Reviews in Mineralogy and Geochemistry*, vol. 70, pp. 47–85, 2009.
- [7] J. S. Lee and J. O. Nriagu, “Stability constants for metal arsenates,” *Environmental Chemistry*, vol. 4, no. 2, pp. 123–133, 2007.
- [8] B. Planer-Friedrich, M. A. Armienta, and B. J. Merkel, “Origin of arsenic in the groundwater of the Rioverde basin, Mexico,” *Environmental Geology*, vol. 40, no. 10, pp. 1290–1298, 2001.
- [9] Y. Zhu, X. Zhang, Q. Xie et al., “Solubility and stability of barium arsenate and barium hydrogen arsenate at 25°C,” *Journal of Hazardous Materials*, vol. 120, no. 1–3, pp. 37–44, 2005.
- [10] R. G. Robins, “The solubility of barium arsenate: sherritt’s barium arsenate process,” *Metallurgical Transactions B*, vol. 16, no. 2, pp. 404–406, 1985.
- [11] L. Méndez-Rodríguez, T. Zenteno-Savín, B. Acosta-Vargas, J. Wurl, and M. Imaz-Lamadrid, “Differences in arsenic, molybdenum, barium, and other physicochemical relationships in groundwater between sites with and without mining activities,” *Natural Science*, vol. 5, pp. 238–243, 2013.
- [12] L. Tiruta-Barna, Z. Rakotoarisoa, and J. Méhu, “Assessment of the multi-scale leaching behaviour of compacted coal fly ash,” *Journal of Hazardous Materials*, vol. 137, no. 3, pp. 1466–1478, 2006.
- [13] H. Binas and K. Boll-Dornberger, “The structure of  $\text{CaHAsO}_4 \cdot \text{H}_2\text{O}$  (haidingerite) and  $\text{SrHAsO}_4 \cdot \text{H}_2\text{O}$ ,” *Chemie der Erde/Geochemistry*, vol. 21, p. 450, 1962.
- [14] C. Martin, A. Durif, and M. T. Adverbuch-Pouchot, “Sur le groupe spatial de l’haidingerite. Données cristallographiques sur  $\text{BaHAsO}_4 \cdot \text{H}_2\text{O}$ ,” *Bulletin Societe Francaise Mineralogie Cristallographie*, vol. 93, p. 397, 1970.
- [15] M. E. Essington, “Solubility of barium arsenate,” *Soil Science Society of America Journal*, vol. 52, no. 6, pp. 1566–1570, 1988.
- [16] C. T. Itoh and K. Tozawa, “Equilibria of the barium(II)-arsenic(III,V) water system at 25°C,” *Tohoku Daigaku Senko Seiren Kenkyusho Iho*, vol. 45, p. 105, 1989.
- [17] F. Orellana, E. Ahumada, C. Suarez, G. Cote, and H. Lizama, “Thermodynamics studies of parameters involved in the formation of arsenic(V) precipitates with barium(II),” *Boletín de la Sociedad Chilena de Química*, vol. 45, pp. 415–422, 2000.
- [18] J. Davis, “Stability of metal-arsenic solids in drinking water systems,” *Practice Periodical of Hazardous, Toxic, and Radioactive Waste Management*, vol. 4, no. 1, pp. 31–35, 2000.
- [19] D. L. Parkhurst and C. A. J. Appelo, “Description of input and examples for PHREEQC version 3—a computer program for speciation, batch-reaction, one-dimensional transport, and inverse geochemical calculations,” in *U.S. Geological Survey Techniques and Methods, Book 6*, chapter A43, pp. 1–497, 2013.
- [20] V. G. Chukhlantsev, “Solubility-products of arsenates,” *Journal of Inorganic Chemistry*, vol. 1, pp. 1975–1982, 1956.
- [21] P. D. Glynn, E. J. Reardon, L. N. Plummer, and E. Busenberg, “Reaction paths and equilibrium end-points in solid-solution aqueous-solution systems,” *Geochimica et Cosmochimica Acta*, vol. 54, no. 2, pp. 267–282, 1990.
- [22] H. Gamsjäger, E. Königsberger, and W. Preis, “Lippmann diagrams: theory and application to carbonate systems,” *Aquatic Geochemistry*, vol. 6, pp. 119–132, 2000.
- [23] D. Baron and C. D. Palmer, “Solid-solution aqueous-solution reactions between jarosite  $(\text{KFe}_3(\text{SO}_4)_2(\text{OH})_6)$  and its chromate analog,” *Geochimica et Cosmochimica Acta*, vol. 66, no. 16, pp. 2841–2853, 2002.



**Hindawi**

Submit your manuscripts at  
<http://www.hindawi.com>

